

# A PHASE FIELD BASED DEEP LEARNING APPROACH FOR MECHANICAL PROPERTY PREDICTION OF SINTERED SILVER IN POWER ELECTRONICS

Borui Yang<sup>1</sup>, Bo Wan<sup>1</sup>, Guicui Fu<sup>1</sup>, Xiaohong Wang<sup>1</sup>, Xiaohui Wang<sup>1</sup>, & Jun Yao<sup>1</sup>

<sup>1</sup>School of Reliability and Systems Engineering, Beihang University, Beijing, China

#### **Abstract**

Sintered silver has a wide range of promising packaging applications in power electronics because of its superior mechanical properties, thermal conductivity. However, it contains pore structures induced by sintering process which significantly affect its mechanical properties. Research on predicting this effect is therefore essential for reliable applications in power electronics. In this paper, tensile test simulation is carried out and mechanical properties are obtained for sintered silver containing pore structure through fracture phase field and finite element method. Based on the data set generated from simulation, a deep learning network structure based on residual network structure and attention mechanism module is established. The network is trained and enhanced by hyperparameter optimization and structure fine-tuning. The proposed deep learning network achieves precise prediction of yield stress, ultimate tensile strength and fracture strain of sintered silver samples with different pore structures. The method provides an effective support for the prediction of pore structure mechanical properties, which significantly save the time consumed in experiments and simulations.

**Keywords:** sintered silver; mechanical property prediction; deep learning; phase field simulation

#### 1. Introduction

As an advanced electronic packaging material, sintered silver can be used in high-power electronic devices, high-end optoelectronic devices and flexible electronic devices. Sintered silver has superior thermal conductivity and mechanical properties. Moreover, the low-temperature sintered interconnect technology for sintered silver can realize the electrical interconnection between the chip and the substrate in a low-temperature and pressure-free environment [1]. Currently, domestic and foreign scholars have carried out effective research on the application of sintered silver and its reliability [2-5]. The high-energy free surface of silver enables sintering at about 200 °C. Thus, the sintering temperature is much lower than its melting point [6]. The low temperature sintering process reduces chip damage. However, the occurrence of pores in the bonding structure is unavoidable. During lowtemperature sintering, the necking process produces a large number of unfilled regions in the material. As a result, a large number of randomly shaped pore structures exist in the interconnect structure formed by sintering. The pore structure has a great impact on the mechanical properties of the electronic interconnect structure. Tests on the mechanical, thermal and electrical properties of chips show that the spatial distribution characteristics of the random pore structures inside the sintered silver interconnect structures have a significant impact on their mechanical, thermal and electrical properties [3,7]. And the mechanical properties are crucial for the performance of solder in service. Crack defects inevitably appear in sintered silver interconnect structures under long-term complex and alternating thermal environments.

The relationship between the pore structure and the mechanical properties of sintered silver is imperative in the development of sintered silver applications. Studies have been conducted to explore

the quantitative relationship between porosity and mechanical behavior [8,9]. Carr et al. investigated the quantitative relationship between porosity and elastic modulus through a combination of simulation and experiment methods [10]. The finite element model was created based on images obtained from scanning electron microscope images of silver layer sections. The modulus of elasticity predicted by the simulation of this study agrees with the experimental measurements. Obviously in practical studies, tensile tests are needed in order to obtain mechanical characterization parameters of sintered silver such as elastic modulus, yield strength, ultimate tensile strength, and fracture strain. However, experiments are costly in terms of manpower and financial resources. Therefore, simulation is an important method used in related materials science in order to achieve efficient research. In recent years, with the development of computer science, numerical methods based on computational mechanics have been successfully applied to fracture analysis [11]. Among the related methods, the phase field method well simulates the process of material tensile fracture by establishing a brittle fracture analysis formula. The fracture phase-field method provides an efficient description of the fracture evolution inside various types of homogenized materials. Cho et al. described the multi-crack sprouting and extension behavior inside laminated composites based on the fracture phase-field model, which demonstrated the validity of the fracture phase-field model [12]. Pillai et al. investigated an efficient prediction method of fracture sprouting and extension inside materials with a random pore structure. combining the macroscopic theory of pore materials and phase field modeling. The method was applied to the simulation of the macroscopic mechanical behavior of pore materials [13]. Under complex thermal or mechanical stresses, a large number of fractures can be generated inside the sintered silver in interconnect structures. Therefore, the phase field method is suitable to be used to study the tensile process of sintered silver containing pore structures.

However, the time consumption of simulation solving computations for mechanical properties of materials is not negligible. In recent years, with the development of machine learning methods, regression tasks for fast prediction of parameters have been realized. Deep learning is one of the methods with outstanding advantages. Typical applications include PHM [14-16], target detection [17,18]. Such methods have also been successfully applied in the field of material parameter prediction. P. Narloch et al. used deep convolutional neural networks to achieve the prediction of compressive strength of cement-stabilized compacted soil, based on scanning electron microscope images [19]. R. Cui et al. used U-net and convolutional neural networks to achieve the prediction of elasticity parameters of rock images [20]. Deep learning methods can adapt well to the nonlinear relationship between input and output parameters. This makes its prediction performance better, compared with traditional modeling prediction methods. Deep learning methods represented by convolutional neural networks exhibit advantages in the data-sufficient situation. When the input of the task is high dimensional, the input contains information that cannot be fully absorbed by traditional modeling methods and machine learning methods. As a result, the phenomenon of dimensionality explosion emerges. Convolutional neural networks solve this problem well through convolutional kernels. Moreover, machine learning and deep learning methods have been effectively used in the field of phase field simulation. One of the application ideas is to accelerate the solution of phase field simulation. C. Hu et al. use principal component analysis (PCA) and long short-term memory network (LSTM) to learn the evolution of microstructure phase field images in the time domain. Highly accurate simulation acceleration was achieved by predicting the simulation results through LSTM [21]. S. Goswami et al. proposed a physical informative neural network (PINN) algorithm based on transfer learning to solve brittle fracture simulations. The output of this method is consistent with the experimental results in six brittle fracture cases [22]. Another idea is to use machine learning or deep learning as a direct alternative to phase field simulation for the prediction of the required parameters. PC. Vilalta et al. successfully used machine learning methods to predict the yield stress in high entropy alloys based on the dataset of the variations of the stacking fault energy landscape [23]. SZ. Feng et al. used the simulation results of the fracture phase field method with a convolutional neural network to achieve the prediction of the remaining useful life of the structure [11]. A Cheloee Darabi et al. used the simulation method combining the phase field method and the finite element method to

generate a dataset of the microstructural and mechanical behaviors of duplex steels under different heat treatment conditions. The prediction of yield stress, ultimate stress and fracture stress of dual-phase steel was realized based on ResNet and VGG16 [24]. However, no study has attempted to predict the mechanical properties of sintered silver containing porous structure by machine learning or deep learning methods.

Thus, in this paper, we propose a predicting approach for mechanical properties of sintered silver containing porous structures based on phase field simulation and neural network method. Satisfying results are achieved in prediction accuracy. This method can significantly save the time consumed in experiments and simulations and facilitate power electronics packaging applications of sintered silver.

# 2. Data Generation

#### 2.1 Phase Field Method

The papers should be prepared, if possible, using the format like this document.

The phase field method developed by Miehe for fracture simulation is used in our research [25,26]. For a system with cracks, the total internal potential energy is consisted of the bulk energy and the energy required for the formation of cracks, which is expressed as

$$W_{\rm int} = \int_{V} \left[ (1 - \phi)^2 + k \right] \psi(\varepsilon) dV + \int_{V} \frac{G_c}{2} \left[ l_0 \nabla \phi \cdot \nabla \phi + \frac{1}{l_0} \phi^2 \right] dV . \tag{1}$$

In the above equation, k is a parameter chosen for numerical convenience. Its value is taken as small as possible while keeping the system of equations is well conditioned. The parameter  $G_c$  is the critical energy release for unstable crack damage extension which is a material property.  $\phi \in [0, 1]$  is the phase field variable that represents the fracture state.  $\Psi(\varepsilon)$  is the strain energy.

The external power energy  $W_{ext}$  are:

$$W_{ext} = \int_{V} \mathbf{b} \cdot \mathbf{u} dV + \int_{\partial V} \mathbf{h} \cdot \mathbf{u} \partial V, \qquad (2)$$

in which b and h are the components of body forces and boundary tractions on the surfaces  $\partial V$ , respectively.

Requiring that  $\delta W_{int}$  -  $\delta W_{ext}$  = 0. We have:

$$\iint_{V} \left[ (1 - \phi)^{2} + k \right] \cdot \boldsymbol{\sigma}_{0} : \delta \boldsymbol{\varepsilon} dV + \int_{V} -2(1 - \phi) \cdot \delta \phi \cdot \psi_{0}(\boldsymbol{\varepsilon}) dV 
+ \int_{V} G_{c} \left( \frac{1}{l_{0}} \phi \cdot \delta \phi + l_{0} \nabla \phi \cdot \nabla (\delta \phi) \right) dV - \int_{V} \boldsymbol{b} \cdot \delta \boldsymbol{u} dV - \int_{\partial V} \boldsymbol{h} \cdot \delta \boldsymbol{u} dA = 0$$
(3)

According to the above equation, the residual vectors of the phase field and the displacement can be obtained separately, for the displacement:

$$R_e^u = \int_V \left[ (1 - \phi)^2 + k \right] \left( B_i^u \right)^T \sigma dV - \int_V N^T b dV - \int_{\partial V} N^T h \partial V . \tag{4}$$

The resulting residual term for the internal energy is:

$$R_{e}^{\phi} = \int_{V} \left[ G_{c} l_{0} \left( B_{i}^{\phi} \right)^{T} \nabla \phi + \left( \frac{G_{c}}{l_{0}} + 2\psi(\varepsilon) \right) N \phi - 2N \psi(\varepsilon) \right] dV, \qquad (5)$$

where N is the FEM shape function matrix and B denotes the gradient matrix. For crack growth analysis, the coupled nonlinear system can be solved through Newton-Raphson iteration, which is expressed as:

$$\begin{cases} \phi \\ u \end{cases}_{n+1} = \begin{cases} \phi \\ u \end{cases}_n - \begin{bmatrix} K_{\phi} & 0 \\ 0 & K_u \end{bmatrix}_n^{-1} \begin{cases} R_e^{\phi} \\ R_e^{u} \end{cases}_n,$$
(6)

where

$$K_{u} = \int_{V} \left[ (1 - \phi)^{2} + k \right] \left( B_{i}^{u} \right)^{T} C B_{j}^{u} dV , \qquad (7)$$

$$K_{\phi} = \int_{V} G_{c} l_{0} \left( B_{i}^{\phi} \right)^{T} B_{j}^{\phi} + \left( \frac{G_{c}}{l_{0}} + 2\psi(\varepsilon) \right) N_{i} N_{j} dV, \qquad (8)$$

The above equations can be solved by making  $R_e^{\phi}=0$  and  $R_e^u=0$  in a staggered system. The Newton-Raphson method is employed in this work to solve the above nonlinear equations. The staggered scheme was utilized with Abaqus Standard [27]. In each calculation step, the obtained information of displacement field and phase field will be preserved in the form of calculating data, which can generate cracks on the input samples in the form of images and stress-strain curves for mechanical properties.

# 2.2 Tensile Test Simulation for Sintered Silver

Before carrying out tensile tests, it is first necessary to generate images of sintered silver samples with random pore structures. In this paper, random pore structure images are generated based on the method of [28]. The image size is 100×100 pixels, as shown in Figure 1. Where, white color is silver and black color is pores. The pore binary images were entered as coordinates of silver and pores into an input file in Abaqus for sample generation in the simulation software.

After importing the samples, a two-dimensional plane model can be created. Uniaxial tensile tests are simulated on the basis of this model after assigning material parameters to the sample. The material parameters of the displacement field for silver and porosity are set as in Table 1. The phase field parameter settings are also included in Table 1 as well. The side length L of the samples are set to 0.02 mm. The bottom of the sample is fixedly constrained in the X and Y directions, while the top is allowed to displace in the Y direction. The simulation is performed using static displacement analysis. A total of 400 incremental steps are set up, and the upper edge displacement for each step is  $\Delta U = 10^{-3} \mu m$ .

Table 1. Parameters setting for fracture simulation

<u> </u>				
		Ag	Pores	
	Elastic modulus	81500 (MPa)	8.15×10 <sup>-5</sup> (MPa)	
	Poisson's ratio	0.38	0.38	
Displacement field	Initial yield strength	275 (MPa)	/	
	Hardening modulus	8150 (MPa)	/	
	Length-scale	0.0004 (mm)		
Phase field	Critical energy release rate	0.016 (N/mm)		



Figure 1. The image of sintered silver with pore structures

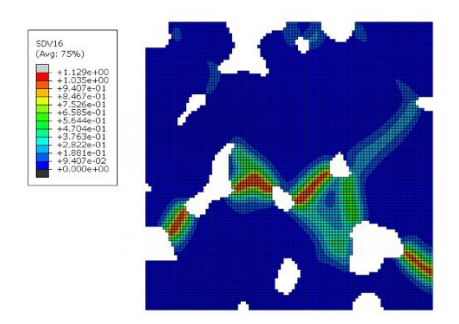


Figure 2. The fracture phase field simulation result of a porous sintered silver sample

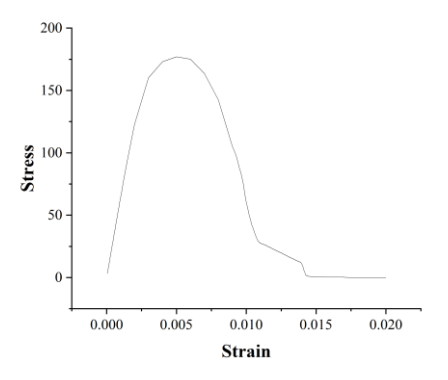


Figure 3. The stress-strain curve of a porous sintered silver sample

# 2.3 Dataset Preparation

Based on the tensile test simulation in the previous section, the batch simulation can be realized by looping the input file. The simulation outputs are the fracture process of the samples under continuous loading with tensile displacement as well as the stress and strain simulation results of the samples. The fracture phase field simulation result of a porous sintered silver sample is shown in Figure 2. The red area represents the fracture region. Based on the simulation results, stress-strain curves are generated as Figure 3. From the stress-strain curve, yield strength, ultimate tensile strength, and fracture strain can be extracted. In the generated dataset, the data samples are images of sintered silver containing pore structures. Its corresponding labels are normalized 3x1 vectors containing yield strength, ultimate tensile strength, and fracture strain from the stress-strain curve. The sample size of the dataset is 7000.

# 3. Deep Learning Method

#### 3.1 Network Framework

Papers are accepted on the basis that they may be edited for style and language. The author himself is responsible for the correctness of the scientific content.

Abbreviations should be spelt out in full the first time they appear and their abbreviated form included in brackets immediately after. Words used in a special context should appear between single quotation marks the first time they appear.

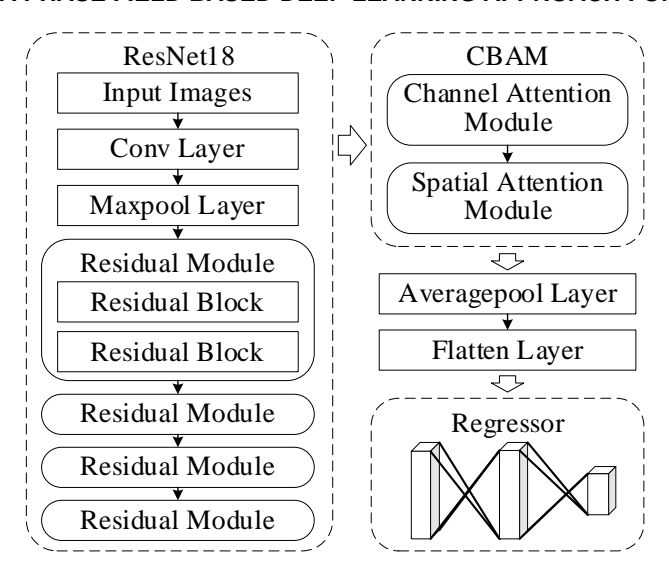


Figure 4. The framework of proposed network

The aim of this paper is to present an image and three mechanical properties of sintered silver containing pore structures obtained based on phase field simulations. They are used as input image features and labels for training and testing, respectively. The mechanical properties include yield strength, ultimate tensile strength, and fracture strain.

We built a deep learning model with ResNet18+CBAM. Sintered silver images containing pore structures are used as input. Firstly, the input is processed through feature extraction by ResNet18 network. ResNet18 consists of 4 residual blocks. After that, the feature maps are fed into the CBAM attention module. The channel features and spatial features of feature maps are enhanced by CBAM module. After average pooling operation and flatten operation, the feature maps are downscaled into 1D vectors and fed into the fully connected layer. Through the mapping of the fully connected layer, the final 1x3 vector is output as the prediction result. During training, based on the prediction results and the actual labels, the loss is computed by a loss function. Adam optimizer is used to implement the backpropagation. Adam optimizer has been proved to be one of the best methods based on the adaptive gradient. The advantage of Adam optimizer is that it maintains the momentum of the previous gradient, which leads to better estimation of the direction of the gradient update. Adam optimizer is more adaptive to different learning rates. is better. Also, it has high stability in the convergence process. Figure 4 illustrates the deep learning model proposed in this paper.

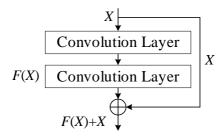


Figure 5. The structure of residual block

ResNet network is proved to be effective deep learning network structure. It uses residual block structure for residual learning of features. The residual block structure is shown in Figure 5. Residual learning solves the problem that deep networks are difficult to train. Deep neural networks have the problem of vanishing or exploding gradients. The idea of residual learning is to ensure that the performance of the network at least does not degrade. Assuming an input of x, the residual block is implemented as F(x)+x. This ensures that the network structure does not lose at least some of its learned features as it passes through the block. Whereas in practice the residual block tends to learn the residual features while preserving the original features. This makes it easier to optimize the

training of deep networks. The input image in this paper is a single channel black and white image with relatively less feature information. Therefore, we choose to construct an 18-layer ResNet structure. Meanwhile, the number of input channels of the initial convolutional layer is set to 1 to adapt to the single-channel image in this paper.

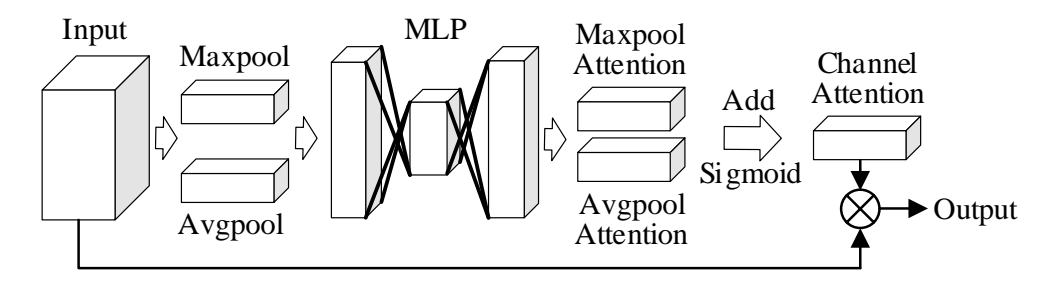


Figure 6. The structure of channel attention module

After the ResNet structure, we use Convolutional Block Attention Module (CBAM) to enhance the information of feature maps through the attention mechanism. CBAM contains the channel attention module and spatial attention module. The structure of the channel attention module is shown in Figure 6. First the feature maps are subjected to average pooling and maximum pooling operations. This allows the spatial information of the feature maps to be aggregated and compressed. The average pooling feature  $F_{avg}$  and the maximum pooling feature  $F_{max}$  are generated separately. Then the Multilayer Perceptual Machine (MLP) is built, which is shared by both  $F_{avg}$  and  $F_{max}$ . The MLP consists of three layers. The dimensions of the first and third layers are the same as the feature vectors. The second layer dimension is reduced to decrease the computational effort while extracting the channel features. After mapping by the MLP layers,  $F_{avg}$  and  $F_{max}$  are merged by element-wise addition. Channel attention values are obtained using the sigmoid layer. The final channel information enhanced feature map is obtained by channel-wise multiplication of the original feature map with the channel attention value.

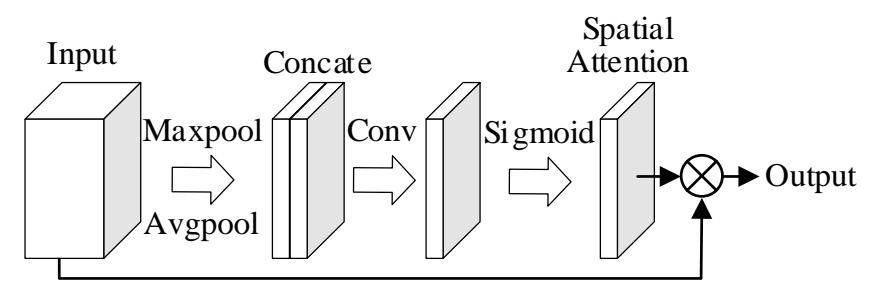


Figure 7. The structure of spatial attention module

The structure of the spatial attention module is shown in Figure 7. The spatial attention module compresses channel features through global average pooling of channels as well as global maximum pooling operations. Two feature maps  $F_{avg}$  and  $F_{max}$  representing different information are generated and merged by concatenation operation. Subsequently, spatial feature extraction is performed on the feature maps by a 7×7 convolution with a large sense field. Finally, the weight map is generated by a sigmoid operation and assigned to the original input feature map by channel-wise multiplication, which allows the target region to be enhanced.

Overall, for spatial attention, the information interaction between channels is ignored as the features in each channel are treated equally. Channel attention, on the other hand, directly processes the information within a channel globally, ignoring the information interactions within the space. The tandem connection of the two modules realizes the enhancement of the input channel information and spatial information.

The regressor in the network of this paper is realized through fully connected layers. The first dimension of the fully connected layer is the same as the input feature vector. The output vector is

a 1×3 prediction of the mechanical properties. The number of layers and neurons in the intermediate layer are parameters that are necessary to regulate. Through the intermediate layer of the fully connected layer, a high-dimensional mapping of the input features to the target labeling can be established. Therefore, these parameters will potentially affect the prediction performance of the neural network. After the fully connected layer outputs the prediction results, the loss is computed by the loss function, which is used to update the parameters of each node of the network by back propagation. In this paper, the logarithmic hyperbolic cosine loss function is utilized. This function is able to combine the fast convergence of the MAE loss and the derivability of the MSE loss at zero. *L*<sub>log-cosh</sub> is the log-cosh loss function which is given as:

$$L_{log-cosh} = \log\left(\cosh\left(y_p - y\right)\right),\tag{9}$$

where  $y_p$  are the prediction values of source domain samples.

#### 3.2 Evaluation Method

In this paper, model performance is assessed by three evaluation indexes commonly used in regression analysis. The prediction results are evaluated in terms of relative and absolute errors respectively. The evaluation indexes include the mean absolute percentage error (MAPE), the mean absolute error (MAE), and the root mean squared error (RMSE) as follows:

$$MAPE = \frac{1}{n} \sum_{i=1}^{n} \left| \frac{\hat{y}_i - y_i}{y_i} \right|,$$
 (10)

$$MAE = \frac{1}{n} \sum_{i=1}^{n} |\hat{y}_i - y_i|, \qquad (11)$$

$$RMSE = \sqrt{\frac{1}{n} \sum_{i=1}^{n} (\hat{y}_i - y_i)^2},$$
 (12)

where  $y_i$  is the true label.  $\hat{y}_i$  is the predicted value. n is the number of samples.

# 4. Experiment Study

To demonstrate the effectiveness of the model proposed in this paper for the prediction of mechanical properties of sintered silver, experiments based on simulation samples were carried out. The dataset generated from the simulation is divided into training set and test set in the ratio of 9:1. The study of model hyperparameters was carried out by grid search method to determine the optimal hyperparameters of the model. Comparison experiments were also conducted. By comparing the present model with other common deep learning structures, the superiority of the present model in the prediction of mechanical properties of pore images is presented. All the work was done using Python 3.7 in Pytorch framework.

# 4.1 Study of Hyperparameters

In this section, the study of hyperparameters is conducted to determine the appropriate hyperparameters for the model. For our network, the main hyperparameters include the learning rate and batchsize. For each hyperparameter experiment, the other parameter space was set consistent. We used the grid search method to investigate the optimal hyperparameter selection.

Firstly, the gird search for learning rate was conducted. The test average results of 3 labels are shown in Table 2. The table shows that the effect of different learning rates on the model prediction results is huge. When the learning rate is too large as 0.005, the model prediction error is huge. Therefore, too large learning rate is obviously unsuitable. When the learning rate is too small, the prediction error shows a slow increasing trend. This means that too small learning rate may cause the model learning efficiency to be too slow and cannot learn the knowledge of the sample well in the limited number of

iterations. Therefore, the learning rate is chosen to be 0.0005, when the prediction error is the lowest.

Table 2. Average errors of learning rate study

Learning rate	MAPE	MAE	RMSE
0.005	20.31%	0.0926	0.1063
0.0005	3.63%	0.0144	0.0197
0.00005	4.25%	0.0156	0.0210
0.000005	6.53%	0.0246	0.0329

The test average results of batchsize experiments are shown in Table 3. As can be seen from the table, batchsize is not a sensitive hyperparameter. There are only minor fluctuations in the prediction error during its variation. In this case, we choose the parameter with the best prediction effect. Therefore, batchsize is set to be 8.

Table 3. Average errors of batchsize study

Batchsize	Batchsize MAPE		RMSE	
4	<b>4</b> 4.20%		0.0217	
<b>8</b> 3.63%		0.0144	0.0197	
16	<b>16</b> 4.30%		0.0232	
32	4.16%	0.0159	0.0211	

# 4.2 Model comparative analysis

comparative analysis of the models is carried out in this section in order to verify the effectiveness of the proposed model in predicting the mechanical properties of sintered silver. AlexNet and VGG are chosen as the comparative models. Their effectiveness in image processing tasks with neural networks has been widely verified. We set up four different image processing methods as four experimental conditions. The difficulty of the comparison experiments can be increased by flipping, rotating and cropping the images. Therefore, the effectiveness of the model can be fully verified.

The test results of the comparison experiments are shown in Tables 4, 5, 6 and 7. Label 1, 2, and 3 represent yield strength, ultimate tensile strength, and fracture strain respectively. Figures 8, 9 and 10 show the MAPE, MAE and RMSE results of the comparison experiments respectively. From the experiments it can be seen that the proposed model is optimal in all the prediction tasks. AlexNet performs moderately well on tasks 1, 2, and 4, but worst on task 3. However, VGG performs worst in tasks 1, 2 and 4 and also has comparable errors to AlexNet in task 3.

From a task perspective, random horizon filp experiment is a relatively easy task. The MAPE of the proposed method in this paper reaches 3.36%. This is lower than the result of no preprocessing. It indicates that this case enriches the dataset and allows the model to more fully accomplish the learning of information. In contrast, the random rotation experimental task has the largest prediction error for each model. The largest prediction error is for AlexNet's label 3 with a MAPE of 16.11%. This reveals that rotation leads to serious information errors, which makes it difficult for the models to learn effective knowledge for effective mapping of features and labels.

In addition, the prediction accuracy of label 2 is generally higher than the other two labels across tasks. This reflects the fact that the images of pore structures in the dataset contain relatively more information about the ultimate tensile strength. This allows the model to create a better mapping between the images and the ultimate tensile strength. From the point of view of labeling error balance, the balance of the method proposed in this paper is also better than other methods. The difference between the prediction errors of each label is relatively small.

Overall, through the comparison experiments, it can be verified that the deep learning model proposed in this paper can well realize the prediction of mechanical properties of sintered silver pore images.

Table 4. Random horizon filp experiment results

Model		Label 1	Label 2	Label 3
AlexNet	MAPE	5.54%	3.84%	5.61%
	MAE	0.0216	0.0160	0.0219
	RMSE	0.0282	0.0218	0.0286
VGG	MAPE	9.25%	5.97%	9.44%
	MAE	0.0341	0.0238	0.0346
	RMSE	0.0467	0.0344	0.0473
	MAPE	3.81%	2.36%	3.89%
Ours	MAE	0.0159	0.0110	0.0160
	RMSE	0.0216	0.0137	0.0207

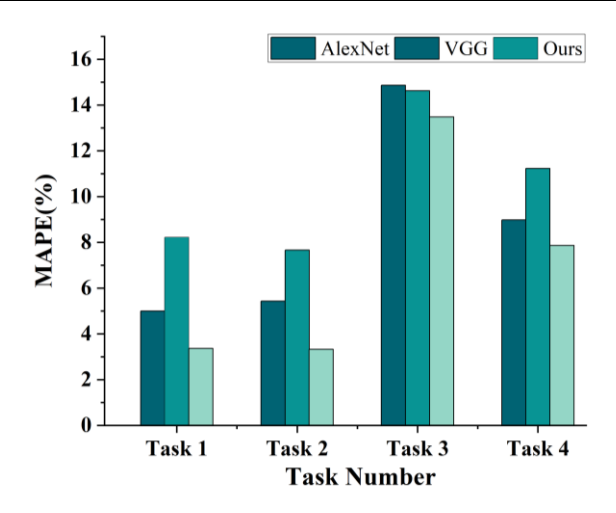


Figure 8. The average MAPE results of comparative experiments

Table 5. Random vertical filp experiment results

Model		Label 1	Label 2	Label 3
AlexNet	MAPE	6.17%	3.90%	6.22%
	MAE	0.0233	0.0158	0.0233
	RMSE	0.0305	0.0217	0.0306
VGG	MAPE	8.94%	5.02%	9.03%
	MAE	0.0341	0.0209	0.0342
	RMSE	0.0450	0.0289	0.0455
	MAPE	3.84%	2.20%	3.91%
Ours	MAE	0.0153	0.0091	0.0155
	RMSE	0.0198	0.0123	0.0201

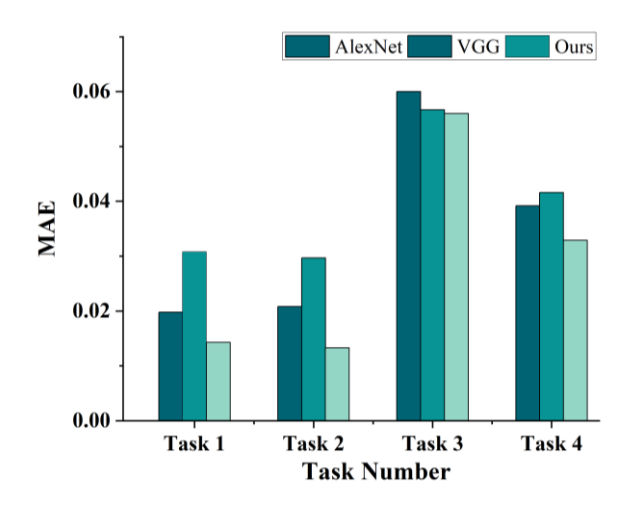


Figure 9. The average MAE results of comparative experiments

Table 6. Random rotation experiment results

Model		Label 1	Label 2	Label 3
AlexNet	MAPE	16.00%	12.46%	16.11%
	MAE	0.0626	0.0548	0.0626
	RMSE	0.0818	0.0732	0.0821
VGG	MAPE	15.68%	12.24%	15.94%
	MAE	0.0585	0.0511	0.0585
	RMSE	0.0779	0.0691	0.0783
Ours	MAPE	14.62%	10.89%	14.92%
	MAE	0.0591	0.0512	0.0597
	RMSE	0.0777	0.0682	0.0785

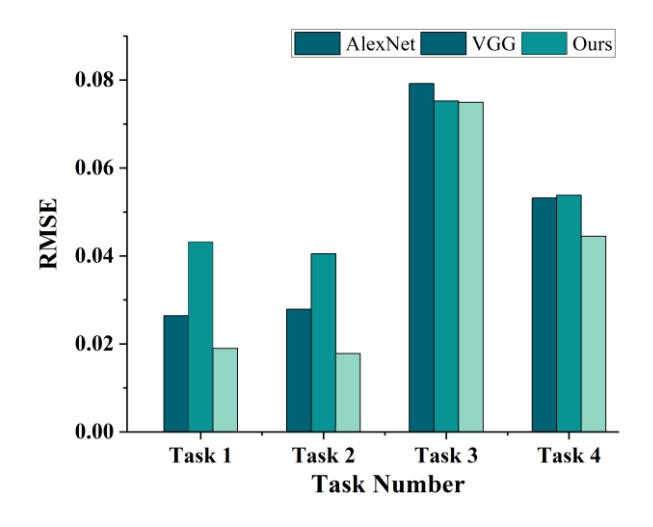


Figure 10. The average RMSE results of comparative experiments

Table 7. Random crop experiment results

Model		Label 1	Label 2	Label 3
	MAPE	965%	7.50%	9.78%
AlexNet	MAE	0.0415	0.0344	0.0416
	RMSE	0.0565	0.0460	0.0565
VGG	MAPE	12.20%	9.10%	12.38%
	MAE	0.0439	0.0366	0.0442
	RMSE	0.0571	0.0493	0.0576
Ours	MAPE	8.33%	6.77%	8.49%
	MAE	0.0343	0.0298	0.0347
	RMSE	0.0463	0.0401	0.0468

### 5. Conclusion

In our research, a mechanical property and corresponding image dataset of porous sintered silver samples is built by fracture phase field simulation. Meanwhile, a deep learning network based on residual network and CBAM attention module is established for realizing the prediction of mechanical properties of porous sintered silver. By hyperparameter analysis, the optimal hyperparameters of the model are determined. In the comparison experiments, the model proposed in this paper is proved to achieve better results under a variety of experimental conditions, compared with the existing excellent models. The proposed deep learning network provides an effective method for the prediction of porous structure mechanical properties, which is sintered silver in this paper for power electronics applications. The results of the study also reflect the feasibility of applying deep learning methods on the prediction of simulation results. In the future, our research will focus on the more accurate application of machine learning and deep learning methods for phase field evolution simulation prediction.

# 6. Copyright Statement

The authors confirm that they, and/or their company or organization, hold copyright on all of the original material included in this paper. The authors also confirm that they have obtained permission, from the copyright holder of any third party material included in this paper, to publish it as part of their paper. The authors confirm that they give permission, or have obtained permission from the copyright holder of this paper, for the publication and distribution of this paper as part of the ICAS proceedings or as individual off-prints from the proceedings.

#### References

- [1] Knoerr, Matthias, Silke Kraft, and Andreas Schletz. Reliability assessment of sintered nano-silver die attachment for power semiconductors. 2010 12th Electronics Packaging Technology Conference. IEEE, 2010.
- [2] Zhao, Su-Yan, et al. Study on high temperature bonding reliability of sintered nano-silver joint on bare copper plate. *Microelectronics Reliability* 55.12 (2015): 2524-2531.
- [3] Khazaka, R., L. Mendizabal, and D. Henry. Review on joint shear strength of nano-silver paste and its long-term high temperature reliability. *Journal of electronic materials* 43 (2014): 2459-2466.
- [4] Jiang, Li, et al. Evaluation of thermal cycling reliability of sintered nanosilver versus soldered joints by curvature measurement. *IEEE Transactions on Components, Packaging and Manufacturing Technology* 4.5 (2014): 751-761.
- [5] Mei, Yun-Hui, et al. Characterization and reliability of sintered nanosilver joints by a rapid current-assisted method for power electronics packaging. *IEEE Transactions on Device and Materials Reliability* 14.1 (2013): 262-267.
- [6] Soichi, Sakamoto, and Katsuaki Suganuma. Low-temperature and low-pressure die bonding using thin

- Ag-flake and Ag-particle pastes for power devices. *IEEE Transactions on Components, Packaging and Manufacturing Technology* 3.6 (2013): 923-929.
- [7] Zhao, Zhenyu, et al. A predictive model for thermal conductivity of nano-Ag sintered interconnect for a SiC die. *Journal of Electronic Materials* 48 (2019): 2811-2825.
- [8] Kimura, Ryo, et al. Effect of sintering temperature on fatigue crack propagation rate of sintered Ag nanoparticles. *Materials Transactions* 59.4 (2018): 612-619.
- [9] Wakamoto, Keisuke, et al. Tensile mechanical properties of sintered porous silver films and their dependence on porosity. *Japanese Journal of Applied Physics* 58.SD (2019): SDDL08.
- [10]Carr, James, et al. Quantitative characterization of porosity and determination of elastic modulus for sintered micro-silver joints. *Journal of Materials processing technology* 225 (2015): 19-23.
- [11]Feng, S. Z., et al. A phase field and deep-learning based approach for accurate prediction of structural residual useful life. *Computer Methods in Applied Mechanics and Engineering* 383 (2021): 113885.
- [12]Cho, Joonyeoun, and Kwan-Soo Lee. Finite element simulation of crack propagation based on phase field theory. *Journal of Mechanical Science and Technology* 27 (2013): 3073-3085.
- [13]Pillai, Udit, Yousef Heider, and Bernd Markert. A diffusive dynamic brittle fracture model for heterogeneous solids and porous materials with implementation using a user-element subroutine. *Computational Materials Science* 153 (2018): 36-47.
- [14] Wang, Pengjun, et al. Device status evaluation method based on deep learning for PHM scenarios. *Electronics* 12.3 (2023): 779.
- [15]Zhao, Lefa, Yafei Zhu, and Tianyu Zhao. Deep learning-based remaining useful life prediction method with transformer module and random forest. *Mathematics* 10.16 (2022): 2921.
- [16]Alghassi, Alireza, Suresh Perinpanayagam, and Mohammad Samie. Stochastic RUL calculation enhanced with TDNN-based IGBT failure modeling. *IEEE Transactions on Reliability* 65.2 (2015): 558-573.
- [17]Chen, Liqiong, Wenxuan Shi, and Dexiang Deng. Improved YOLOv3 based on attention mechanism for fast and accurate ship detection in optical remote sensing images. *Remote Sensing* 13.4 (2021): 660.
- [18]Li, Linhao, et al. Domain adaptive ship detection in optical remote sensing images. *Remote Sensing* 13.16 (2021): 3168.
- [19]Narloch, Piotr, et al. Predicting compressive strength of cement-stabilized rammed earth based on SEM images using computer vision and deep learning. *Applied Sciences* 9.23 (2019): 5131.
- [20]Cui, Rongang, et al. VP and VS prediction from digital rock images using a combination of U-Net and convolutional neural networks. *Geophysics* 86.1 (2021): MR27-MR37.
- [21]Hu, C., S. Martin, and R. Dingreville. Accelerating phase-field predictions via recurrent neural networks learning the microstructure evolution in latent space. *Computer Methods in Applied Mechanics and Engineering* 397 (2022): 115128.
- [22] Goswami, Somdatta, et al. Transfer learning enhanced physics informed neural network for phase-field modeling of fracture. *Theoretical and Applied Fracture Mechanics* 106 (2020): 102447.
- [23] Vilalta, Pau Cutrina, et al. Machine learning for predicting the critical yield stress of high entropy alloys. *Journal of Engineering Materials and Technology* 143.2 (2021): 021005.
- [24] Cheloee Darabi, Ali, et al. Hybrid Data-Driven Deep Learning Framework for Material Mechanical Properties Prediction with the Focus on Dual-Phase Steel Microstructures. *Materials* 16.1 (2023): 447.
- [25]Miehe, Christian, Martina Hofacker, and Fabian Welschinger. A phase field model for rate-independent crack propagation: Robust algorithmic implementation based on operator splits. *Computer Methods in Applied Mechanics and Engineering* 199.45-48 (2010): 2765-2778.
- [26]Miehe, Christian, Fabian Welschinger, and Martina Hofacker. Thermodynamically consistent phase-field models of fracture: Variational principles and multi-field FE implementations. *International journal for numerical methods in engineering* 83.10 (2010): 1273-1311.
- [27] Molnár, Gergely, and Anthony Gravouil. 2D and 3D Abaqus implementation of a robust staggered phase-field solution for modeling brittle fracture. *Finite Elements in Analysis and Design* 130 (2017): 27-38.
- [28]Su, Yutai, et al. Thermo-elasto-plastic phase-field modelling of mechanical behaviours of sintered nano-silver with randomly distributed micro-pores. *Computer Methods in Applied Mechanics and Engineering* 378 (2021): 113729.